ADVANCED MATERIALS

Supporting Information

for *Adv. Mater.*, DOI 10.1002/adma.202304905

Spin–Orbit Torques and Spin Hall Magnetoresistance Generated by Twin-Free and Amorphous $Bi_{0.9}Sb_{0.1}$ Topological Insulator Films

Federico Binda, Stefano Fedel, Santos Francisco Alvarado, Paul Noël and Pietro Gambardella**

Supporting Information to the manuscript
"Spin-orbit torques and spin Hall magnetoresistance generated by twin-free and amorphous $Bi_{0.9}Sb_{0.1}$ topological insulator films"

Federico Binda, Stefano Fedel, Santos Francisco Alvarado, Paul Noël, Pietro Gambardella

Department of Materials, ETH Zurich, CH-8093 Zurich, Switzerland

1 Structural characterization

Figure S1(a) shows the RHEED images of the different layers constituting the twin-free $Bi_{0.9}Sb_{0.1}$/FeCo sample. The left column corresponds to RHEED images taken along the BaF_2 $[10\bar{1}]$ direction, the right column to the BaF_2 $[11\bar{2}]$ direction. The RHEED pattern of $Bi_{0.9}Sb_{0.1}$ becomes more streaky after the annealing step, indicating that the film becomes flatter. On the left column, the RHEED pattern of FeCo displays a rectangular cell which appears rotated by 30°, with the ratio between the sides a and b being close to $\sqrt{2}$. This is compatible with a rotated BCC lattice with the [110] direction pointing out-of-plane. On the right column, the reflexes of the FeCo layer match those of the $Bi_{0.9}Sb_{0.1}$ layer (lattice-matching interface), consistently with a BCC unit cell of FeCo with the [110] direction pointing out-of-plane and the [001] direction (nominal lateral spacing of about 4.1 Å) parallel to the $[10\bar{1}0]$ direction of $Bi_{0.9}Sb_{0.1}$ (nominal lateral spacing of about 4.4 Å). The angle between the two directions along which the RHEED patterns are taken is of 30°, which is consistent to the rotation of 30° of the RHEED pattern attributed to the BBC unit cell.

Figure S1(b) shows the RHEED images of the layers constituting the amorphous $Bi_{0.9}Sb_{0.1}$/FeCo sample. The RHEED patterns of both FeCo and $Bi_{0.9}Sb_{0.1}$ appear with cloudy backgrounds, indicating the growth in the amorphous phase.

Figure S1(c) shows the XRD (0003)reflex of the $Bi_{0.9}Sb_{0.1}$ twin-free layer from the $2\theta/\omega$ scan. A Gaussian fit is used to determine the full width half maximum of the peak. From the peak broadening, we then used the Scherrer formula (shown in the Figure) for determining the crystallite size $\tau = 93\pm5$ Å, compatible with the film nominal thickness.

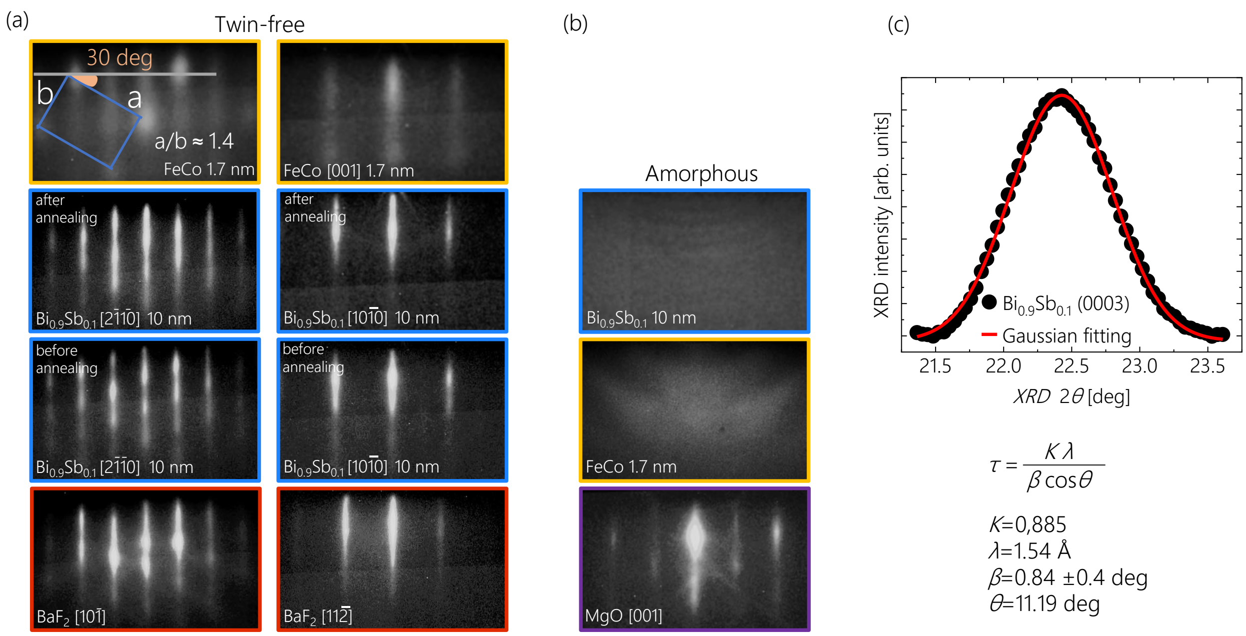

Figure S1: Structural characterization. (a) RHEED pattern of the substrate and layers constituting the twin-free $Bi_{0.9}Sb_{0.1}$/FeCo sample measured with the electron beam incident along the $[10\bar{1}]$ and $[11\bar{2}]$ direction of BaF_2. For the $Bi_{0.9}Sb_{0.1}$ layer, the RHEED image is taken before and after the annealing step. (b) RHEED patterns of the amorphous bilayer. (c) $2\theta/\omega$ XRD scan of the (0003) peak of the twin-free $Bi_{0.9}Sb_{0.1}$ single layer sample (black dots) with Gaussian fit (red line). The fit is used to evaluate the peak broadening from which the crystallite size τ is estimated through the Scherrer equation. K is the dimensionless shape factor, λ is the XRD wavelength, θ is the reflex angle and β is the peak broadening at half the maximum intensity. This value has uncertainty coming from averaging two nominally identical samples. The instrumental peak broadening is not taken into account.

2 Magnetic characterization

We characterized the magnetic properties of the unpatterned samples at room temperature using a superconducting quantum interference device (SQUID) and the longitudinal magneto-optical Kerr effect (L-MOKE). Both samples present in-plane magnetic anisotropy, with the twin-free $Bi_{0.9}Sb_{0.1}$ bilayer sample showing a weak uniaxial magnetic anisotropy in the plane from L-MOKE measurements, in agreement with the crystallographic orientation of FeCo [1] observed by RHEED. However, this uniaxial anisotropy is not detected during magnetotransport measurements of the patterned devices, where the sample shows easy-plane magnetic anisotropy.

Figure S2(a) shows the remanent magnetization of the twin-free $Bi_{0.9}Sb_{0.1}$/FeCo bilayer as measured by the Kerr signal at zero field. These measurements show that the as-grown FeCo layer has a very weak in-plane uniaxial anisotropy, with easy axis roughly oriented along the cubic [001] crystal direction and hard axis along [110]. This agrees with the magnetocrystalline anisotropy of a BCC FeCo crystal with (110) surface normal [1], in agreement with the RHEED results.

In the measurements performed on patterned devices, the uniaxial in-plane magnetic anisotropy is too weak to play a role. This is shown in Figure S2(b) by the derivative of the Hall resistance R_{H} measured as a function of φ_{B} for the twin-free $Bi_{0.9}Sb_{0.1}$/FeCo sample at the minimum external field used, $B_{\mathrm{ext}}\approx 0.3$ T. Here φ_{B} is the in-plane angle of the applied external field measured relative to the current direction. For a sample with in-plane magnetization, R_{H} probes the planar Hall effect, which gives maximum (minimum)

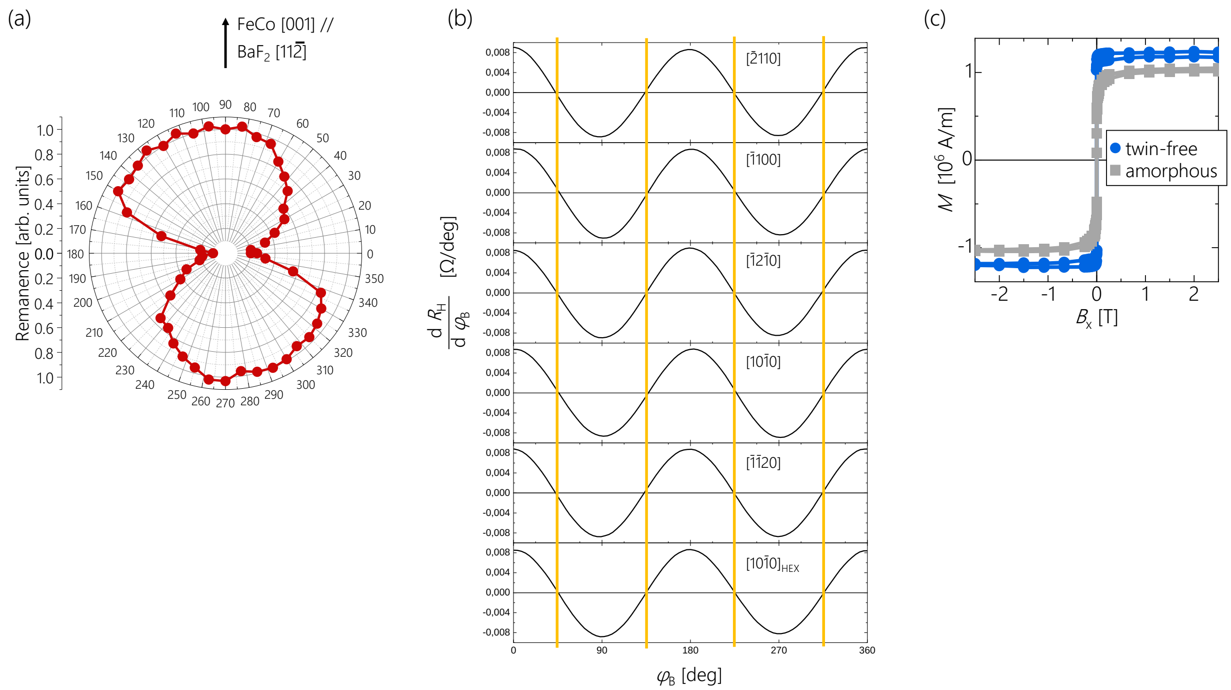

Figure S2: Magnetic characterization of $Bi_{0.9}Sb_{0.1}$/CoFe. (a) L-MOKE data versus in-plane rotation angle of the sample, showing the remanent Kerr rotation signal. (b) Derivative of the Hall resistance R_{H} with respect to the in-plane angle of the applied external field φ_{B} for different device orientations of the twin-free $Bi_{0.9}Sb_{0.1}$/FeCo bilayer. The amplitude of the external field was B_{ext}=0.3 T, with B_{ext} being parallel to the current at φ_{B}=0. R_{H} probes the planar Hall effect, which gives maximum or minimum signal with zero derivative when the magnetization lies at 45° with respect to the current direction. The sample has easy-plane magnetic anisotropy since the derivative data intercept zero exactly every 90°, with the magnetization following the rotating external field independently of the device orientation. (c) Room temperature magnetization of the twin-free $Bi_{0.9}Sb_{0.1}$/FeCo and amorphous bilayers measured by SQUID using an in-plane magnetic field.

signal when the magnetization lies at 45°, 225° (135°, 315°) with respect to the current. The derivative of R_{H} has zeroes at these angles (yellow lines), showing that the magnetization follows the external field when it is rotated in the xy plane, consistently with easy-plane anisotropy.

The magnetization of the as-grown samples was measured using a superconducting quantum interference device (SQUID) at room temperature (see Figure S2(c)). The rectangular shape of the hysteresis curve confirms that the easy axis of the magnetization lies in the plane. The twin-free $Bi_{0.9}Sb_{0.1}$/FeCo bilayer (blue circles) has a saturation magnetization M_{s}=1.1×10^6 A/m and the amorphous bilayer (gray squares) has M_{s}=1×10^6 A/m. Both values smaller than the one expected for bulk BCC FeCo, M_{s}=1.6×10^6 A/m [2]. We attribute this discrepancy to issues common to ultrathin films, such as reduced Curie temperature and possible interface diffusion [3, 4]. The resistivity and magnetic properties of the samples are summarized in Table S1.

Sample	ρ [$\mu\Omega$cm]	ρ_{BiSb} [$\mu\Omega$cm]	ρ_{FeCo} [$\mu\Omega$cm]	$\frac{I_{\mathrm{BiSb}}}{I}$ [%]	M_{s} [10^6A/m]	$B_{\mathrm{ani+dem}}$ [mT]	R_{AHE} [Ω]
Twin-free	235	460	60*	45	1.1	1390	1.8
Amorphous	515	660*	225	67	1.0	770	4.5

Table S1: Summary of the magnetic and electric properties of the twin-free and amorphous $Bi_{0.9}Sb_{0.1}$ samples at room temperature. Resistivity of the bilayer samples and of $Bi_{0.9}Sb_{0.1}$ and FeCo single layers (the data with the asterisk are calculated via parallel resistor model and not measured), current percentage flowing through the $Bi_{0.9}Sb_{0.1}$ layer, saturation magnetization, out-of-plane saturation field, and anomalous Hall resistance.

3 Magnetoresistance of the twin-free single layer and bilayer $Bi_{0.9}Sb_{0.1}$ samples as a function of magnetic field

In heavy metal/ferromagnetic metal bilayer the high values of the ΔRzy indicate strong charge–to-spin conversion and ΔRzx ≈ 0 indicates that the AMR is very small. In topological insulator materials, however, the ordinary (Lorentz) magnetoresistance (OMR) is considerably larger than that of heavy metals possessing a high carrier density. The OMR in a 2D system varies with B_z^2 and has the following contributions: ΔRzy ≈ ΔRzx >0 and ΔRxy ≈ 0. We show in Figure S3 the different angular dependencies of OMR, AMR and SMR [5]. For example, the OMR contribution is dominant in topological insulator/ferrimagnetic insulator bilayers [6], whereas the SMR dominates in a heavy metal/ferrimagnetic insulator bilayers. The OMR contribution can be an issue to properly estimate the SMR if the angular dependent measurement is performed only at a fixed field. Indeed, both the AMR + SMR and AMR + OMR result in ΔRxy ≠ ΔRzy ≠ ΔRzx ≠ 0. In the twin-free $Bi_{0.9}Sb_{0.1}$/FeCo bilayer sample, however, we have ΔRzx ≈ 0, which shows that the contribution of the OMR is negligible. To confirm this point, we measured the magnetoresistance as a function of the out-of-plane field B_z for the twin-free single layer $Bi_{0.9}Sb_{0.1}$ and the $Bi_{0.9}Sb_{0.1}$/FeCo bilayer discussed in the manuscript (Figure S4). The single layer $Bi_{0.9}Sb_{0.1}$ presents a clear OMR signal (see Figure S4(a)), whereas the $Bi_{0.9}Sb_{0.1}$/FeCo bilayer presents no contribution proportional to the square of the field, thus confirming the absence of the OMR (see Figure S4 (b)). Instead, the $Bi_{0.9}Sb_{0.1}$/FeCo bilayer presents a negative magnon magnetoresistance (MMR) at large fields and a dominant SMR signature below 2 T.

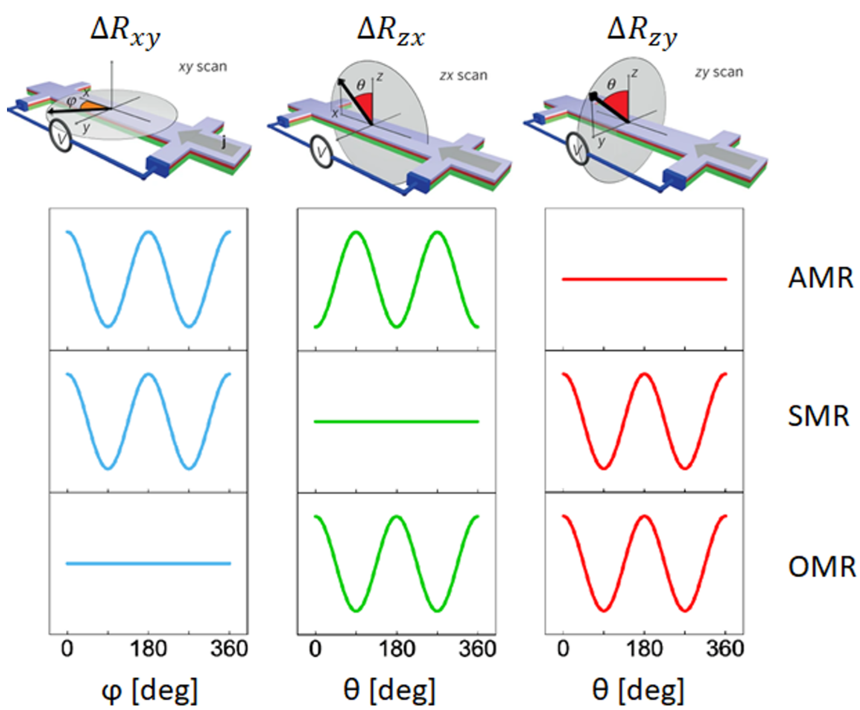

Figure S3: Angular dependence of the AMR, SMR and OMR.

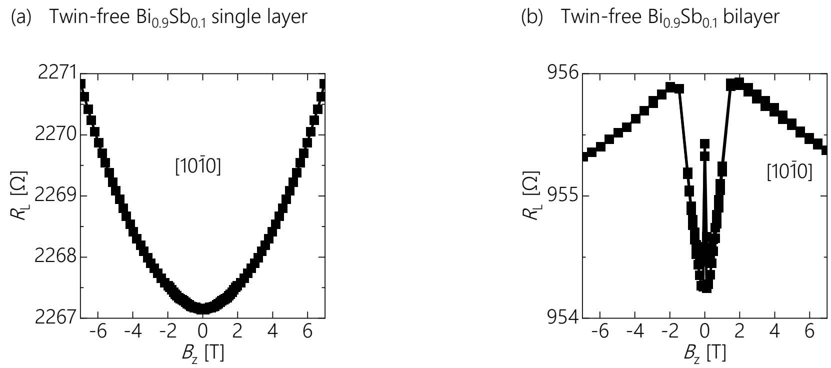

Figure S4: Magnetoresistance of the twin-free single layer $Bi_{0.9}Sb_{0.1}$ and bilayer $Bi_{0.9}Sb_{0.1}$/FeCo measured at room temperature as a function of the out-of-plane field B_z. For both samples, the current was injected along the [10$\bar{1}$0] direction.

4 Second harmonic signal from single layer twin-free $Bi_{0.9}Sb_{0.1}$

Single films of BiSb are known to exhibit a strong ordinary Nernst effect (ONE). Owing to current injection and the consequent thermal gradient induced by Joule heating, the ONE can induce a second harmonic signal in the harmonic Hall voltage measurements of BiSb as the magnetic field is rotated in the xy plane [7]. Another possible contribution to the total second harmonic signal when the field is rotated in the xy plane is the bilinear magnetoelectric resistance (BMER) due to spin-momentum locking in the topological surface states [8] and the related nonlinear planar Hall effect (NLPHE) [9]. These two contributions appear in the longitudinal and transverse directions, respectively. Both effects vary linearly with external magnetic field and can be subtracted from the second harmonic response of the bilayer samples, as described in Section 5 of the Supporting Information. Here, we report the transverse and longitudinal second harmonic resistance of a twin-free $Bi_{0.9}Sb_{0.1}$ single layer sample (Figure S5). The analysis of these data shows that the dominant contribution to the second harmonic response of BiSb is the ONE, which has been taken into account in determining the SOT efficiency of the bilayer samples.

Figures S5(a,b) show the transverse $R_{2\omega,\mathrm{H}}$ and longitudinal $R_{2\omega,\mathrm{L}}$ second harmonic resistances. Both curves can be fitted by simple sinusoidal functions, $\cos\varphi$ for $R_{2\omega,H}$ and $\sin\varphi$ for $R_{2\omega,L}$. The fit amplitudes, $R_{\mathrm{cos,H}}$ and $R_{\mathrm{sin,L}}$, scale linearly with the field, as expected. The 90° shift between the transverse and longitudinal resistances and the linearity with field are typical of the ONE but have been reported also in the presence of BMER and NLPHE [9].

In order to confirm the origin of the signal, we compared the amplitudes of the longitudinal and transverse resistances. We found a ratio $R_{\mathrm{sin,L}}/R_{\mathrm{cos,H}} \approx 6$, comparable to the nominal aspect ratio of 5 of the patterned Hall bar device. A ratio close to the nominal aspect ratio is expected for the ONE, whereas the expected ratio for the BMER and NLPHE contributions would be 15, following results from Ref. [9]. Thus, we conclude that the ONE dominates the second harmonic response of single layer BiSb. The difference between $R_{\mathrm{sin,L}}/R_{\mathrm{cos,H}}$ and the nominal aspect ratio is likely due to slight variations in the device patterning process and a smaller out-of-plane thermal gradient near the Hall contacts due to a better heat dissipation.

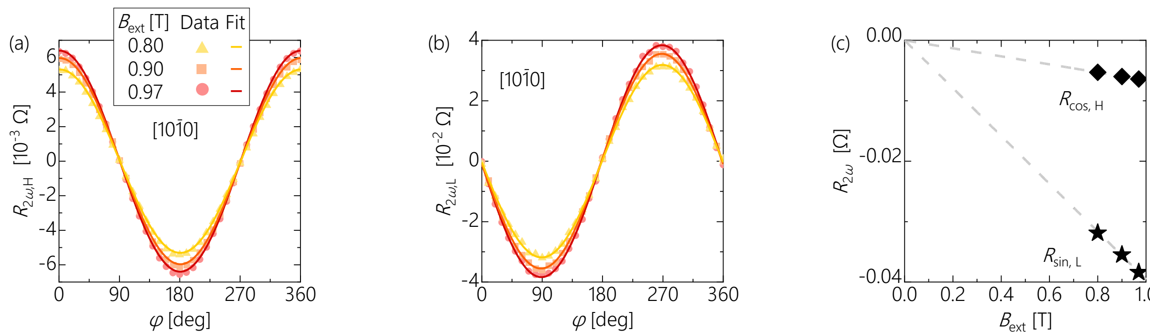

$R_{2\omega,H} = -R_{cos,H} \cos\varphi$

$R_{2\omega,L} = R_{sin,L} \sin\varphi$

(a.r.)= $R_{sin,L} / R_{cos,H}$

with $R_{cos,H} = R_{ONE,H} = c_{ONE}\, B_{ext}$

$c_{ONE,BiSb} = R_{ONE,H} / B_{ext}$

B_{ext} [T]	$R_{cos,H}$ [Ω]	err $R_{cos,H}$ [10^{-5} Ω]
0.80	-0.0053	2
0.90	-0.0060	2
0.97	-0.0064	2.5

B_{ext} [T]	$R_{sin,L}$ [Ω]	err $R_{sin,L}$ [10^{-4} Ω]
0.80	-0.0319	1.42
0.90	-0.0355	1.02
0.97	-0.0384	1.36

B_{ext} [T]	(a.r.)	err (a.r.)	$c_{ONE,BiSb}$ [10^{-3} Ω/T]
0.80	6.02	0.04	-6.63
0.90	5.92	0.03	-6.66
0.97	6.00	0.03	-6.60

Figure S5: Second harmonic Hall resistance of the twin-free $Bi_{0.9}Sb_{0.1}$ single layer sample as a function of the angle of the applied magnetic field in the xy plane. The data are shown for different magnetic fields, with current density $j \approx 4\times10^5$ A/cm^2 applied along [10$\bar{1}$0] at T = 30 K. (a) Transverse $R_{2\omega,H}$ and (b) longitudinal $R_{2\omega,L}$ second harmonic resistance. The fitting functions and parameters $R_{cos,H}$ and $R_{sin,L}$ are reported below the plots. (c) Linear dependence of $R_{cos,H}$ and $R_{sin,L}$ on the field B_{ext}. The table below the plot shows the calculated values of the aspect ratio (a.r.) and the ONE coefficient $c_{ONE,Bisb}$.

5 Spin-orbit torque quantification using Harmonic Hall voltage measurements

The SOTs consist of two components, the fieldlike torque (FL-SOT, including the Oersted field contribution) $\mathbf{T}_{\mathrm{FL+Oe}} \sim \mathbf{m} \times \mathbf{y}$, and the dampinglike torque (DL-SOT), $\mathbf{T}_{\mathrm{DL}} \sim \mathbf{m} \times (\mathbf{y} \times \mathbf{m})$ [10]. These spin torques can be expressed in the form of effective magnetic fields which are accessible experimentally: $\mathbf{B}_{\mathrm{FL+Oe}} \sim \mathbf{y}$ and $\mathbf{B}_{\mathrm{DL}} \sim \mathbf{y} \times \mathbf{m}$. We measured the SOT effective fields using the harmonic Hall voltage method described in detail in Ref. [11]. The technique involves recording the first and the second harmonic Hall resistance under the injection of an a.c. current, as a function of the direction and intensity of an external magnetic field B_{ext}. We present below the step-by-step procedure followed to quantify the SOTs at room temperature for the representative case of the twin-free $\mathrm{Bi}_{0.9}\mathrm{Sb}_{0.1}$/FeCo bilayer.

The first harmonic Hall resistance has contributions from the anomalous Hall (R_{AHE}) and planar Hall effect (R_{PHE}) that can be expressed as a function of the polar and azimuthal magnetization angles θ and φ, respectively:

$$R_{\mathrm{H}} = R_{\mathrm{AHE}} \cos\theta + R_{\mathrm{PHE}} \sin^2\theta \sin 2\varphi. \tag{1}$$

The second harmonic Hall resistance has contributions from the SOTs ($R_{\mathrm{FL+Oe}}$ and R_{DL}), due to the SOT-induced oscillations of the magnetization, and from the magnetothermal effects (R_{ANE} and R_{ONE}), due to the anomalous and ordinary Nernst effects (ANE and ONE) induced by the out-of-plane thermal gradient caused by Joule heating [12, 11]. As the external magnetic field rotates the magnetization in the xy-plane

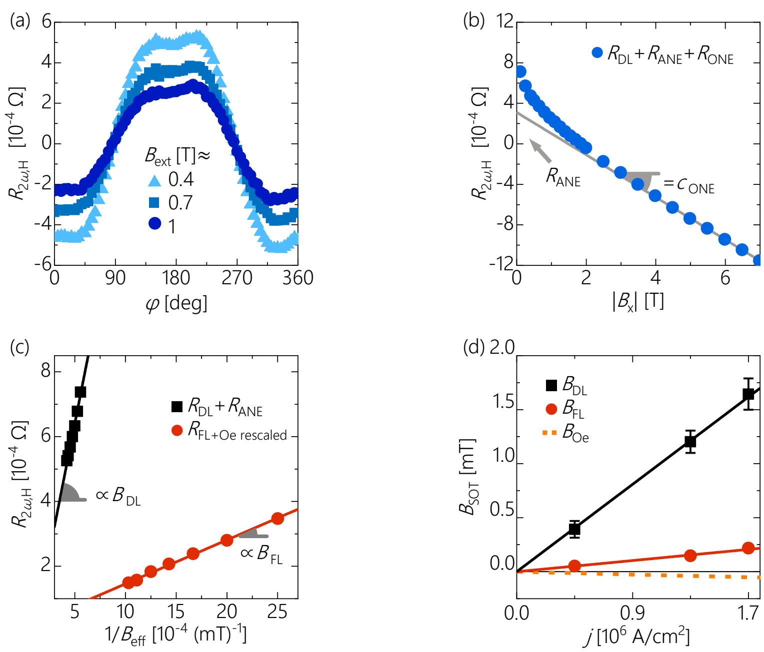

Figure S6: SOT quantification by harmonic Hall voltage measurements at room temperature for the twin-free $\mathrm{Bi}_{0.9}\mathrm{Sn}_{0.1}$ bilayer sample, with the device oriented along $[10\bar{1}0]$. (a) xy angle scan of $R_{2\omega,\mathrm{H}}$ at different external magnetic fields presenting contributions from SOTs and magnetothermal effects. (b) Field scan of $R_{2\omega,\mathrm{H}}$ along x. The slope at high fields corresponds to the ordinary Nernst coefficient c_{ONE}; the intercept with the y-axis to the anomalous Nernst resistance R_{ANE}. (c) FL- and DL-SOT resistances estimated by fitting the data in (a) as a function of the inverse of $(B_{\mathrm{ext}} + B_{\mathrm{ani+dem}})$. (d) FL- and DL-SOT effective fields as a function of the electric current density j. The solid lines are linear fits to the data with the intercept fixed at zero. the dashed line is the estimated Oersted field. The current density in (a), (b) and (c) is j=1.7×10^6 A/cm^2.

(xy angle scan) in a sample with easy-plane anisotropy, the 2nd harmonic Hall resistance can be written as:

$$R_{2\omega,\mathrm{H}} = R_{\mathrm{FL+Oe}}\,(2\cos^3\varphi - \cos\varphi) - (R_{\mathrm{DL}} + R_{\mathrm{ANE}} + R_{\mathrm{ONE}})\cos\varphi. \tag{2}$$

The different φ-dependence of $R_{\mathrm{FL+Oe}}$ and R_{DL} allows for separating the two SOT contributions. However, the extraction of the term R_{DL} is non-trivial since also the magnetothermal effects share the same $\cos\varphi$ dependence [11]. Materials based on Bi, such as most topological insulators, present strong Nernst effects [13]. In such a case R_{DL} is isolated by exploiting the different dependence of the magnetothermal resistances with respect to the magnetic field: whereas R_{ANE} is field-independent, R_{ONE} is linearly proportional to the field, such that $R_{\mathrm{ONE}} = c_{\mathrm{ONE}}\,B_{\mathrm{ext}}$, with the constant c_{ONE} quantifying the strength of the ONE. Such a term can be separated by performing a field scan along x ($\cos\varphi$=1 in Eq. 2) and considering that, at high magnetic field, the SOT contributions are fully suppressed and the slope of the second harmonic Hall resistance is exclusively dominated by the ONE. Once R_{ONE} is known, the coefficients $R_{\mathrm{FL+Oe}}$ and $-(R_{\mathrm{DL}} + R_{\mathrm{ANE}})$ are estimated by simultaneously fitting several xy angle scans at different B_{ext}. Since the increasing external magnetic field progressively suppresses the torques, the effective fields B_{DL} and $B_{\mathrm{FL+Oe}}$ are eventually quantified by exploiting their field dependence [11]: $R_{\mathrm{DL}} = \frac{1}{2}\,\frac{R_{\mathrm{AHE}}}{B_{\mathrm{ext}}+B_{\mathrm{ani+dem}}}\,B_{\mathrm{DL}}$, where $B_{\mathrm{ani+dem}}$ is the sum of the effective anisotropy field and the demagnetizing contribution, and $R_{\mathrm{FL+Oe}} = \frac{1}{2}\,\frac{R_{\mathrm{PHE}}}{B_{\mathrm{ext}}}\,B_{\mathrm{FL+Oe}}$.

Figure S6 groups all the experimental data used for the SOT measurements in the twin-free $\mathrm{Bi_{0.9}Sb_{0.1}}$/FeCo bilayer for a device oriented along the $[10\bar{1}0]$ direction. Figure S6(a) shows the room-temperature second harmonic Hall resistance data for xy angle scans at three representative fields with j=1.7×10^6 A/cm^2. We fitted $R_{2\omega,\mathrm{H}}$ using Eq. 2, finding the coefficients $R_{\mathrm{FL+Oe}}$ and -($R_{\mathrm{DL}} + R_{\mathrm{ANE}} + R_{\mathrm{ONE}}$). To estimate R_{ONE} at different fields, we determined c_{ONE} by fitting the slope of $R_{2\omega,\mathrm{H}}$ as a function of the external magnetic field along x for B_{ext} >4 T, as shown in Figure S6(b). In this plot, the intercept of the fit with the y-axis corresponds to R_{ANE}, which depends exclusively on the magnetization and not on the field. We then subtracted R_{ONE} from -($R_{\mathrm{DL}} + R_{\mathrm{ANE}} + R_{\mathrm{ONE}}$) and plotted ($R_{\mathrm{DL}} + R_{\mathrm{ANE}}$) versus $1/(B_{\mathrm{ext}} + B_{\mathrm{ani+dem}})$, as shown in Figure S6(c). This plot allows us to finally evaluate B_{DL}, which corresponds to the slope of the linear fit divided by $\frac{R_{\mathrm{AHE}}}{2}$.

We quantified the FL-SOT by exploiting the field-dependent relation described above. Figure S6(c) presents $R_{\mathrm{FL+Oe}}$ versus $\frac{1}{B_{\mathrm{ext}}}$ (red dots), with each data point rescaled by a factor $\frac{R_{\mathrm{PHE}}}{\max(R_{\mathrm{PHE}})}$ to account for the varying R_{PHE} at different B_{ext}, with $\max(R_{\mathrm{PHE}})$ being the maximum value of R_{PHE}. In this type of plot, $B_{\mathrm{FL+Oe}}$ corresponds to the slope of the fit (red dashed line) divided by $\frac{\max(R_{\mathrm{PHE}})}{2}$. Next, to determine B_{FL}, we subtracted the calculated Oersted field B_{Oe} from $B_{\mathrm{FL+Oe}}$, taking $B_{\mathrm{Oe}} = \frac{\mu_0 I_{\mathrm{BiSb}}}{2w}$, where μ_0 is the vacuum permeability, w the current line width and I_{BiSb} the current flowing in the nonmagnetic layer. Figure S6(d) finally shows B_{DL} and B_{FL} as a function of injected current density j. The agreement between data and fit proves the linear relation between the SOT and the injected current.

6 Temperature calibration

The current density used to measure the SOT is relatively large, causing non-negligible Joule heating at low temperature. We thus calibrated the sample temperature by comparing the temperature-dependent longitudinal resistance of the $Bi_{0.9}Sb_{0.1}$/FeCo bilayer measured with j=1.7×10^6 A/cm^2, corresponding to a dissipated power of 4 mW, and j=4×10^4 A/cm, corresponding to a dissipated power of 2.4×10^{-3} mW. Assuming that in the latter case the nominal temperature is equal to the real temperature, we can calibrate the temperature of the high current measurements by equating the resistance in the two cases. Figure S7(a) shows that, regardless of the different dissipated power, the two longitudinal resistance presents a similar temperature-dependent behavior between 300 and 50 K. This indicates that the nominal temperature is very close to the real temperature. Figure S7(b) shows the temperature correction performed below 30 K.

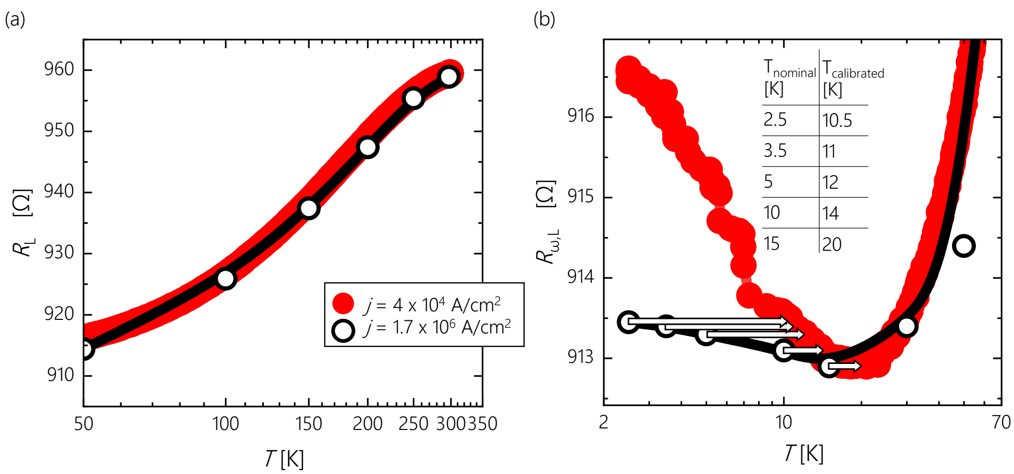

Figure S7: Temperature dependence of the longitudinal resistance of the twin-free $Bi_{0.9}Sb_{0.1}$/FeCo bilayer for a device oriented along [10$\bar{1}$0] with j=1.7×10^6 A/cm^2 (open dots) and j=4×10^4 A/cm^2 (red dots). (a) The data measured between 300 and 50 K indicate good agreement between the nominal and real sample temperature. (b) Below 30 K the nominal temperature of the high current measurement must be corrected to match the resistance measured at low current.

7 Weak antilocalization

In the twin-free $Bi_{0.9}Sb_{0.1}$ we observed an increase of the magnetoresistance at low temperature when the field is applied along the perpendicular direction z. The magnetoresistance is positive and has a cusp shape typical of the weak antilocalization (WAL) as can be seen in Figure 5(e) of the main text. To understand the dimensionality of the WAL, we measured the change of resistance for different angles as a function of the magnetic field projection along the film normal $B_z = B_{ext} \cos\theta$ at 2.5 K, where θ is the angle between the surface normal and the applied magnetic field. As can be seen in Figure S8 (a) the curves overlap, which is the signature of the two-dimensional (2D) origin of the WAL [14].

In a topological insulator the magnetoconductance $\Delta\sigma$ can be fitted using the Hikami-Larkin-Nagaoka (HLN) two-dimensional quantum diffusion model [15] in the high spin-orbit coupling limit:

$$\Delta\sigma = -\frac{\alpha e^2}{2\pi^2\hbar}\left[\Psi\left(\frac{\hbar}{4eB_zL_\varphi^2}+\frac{1}{2}\right)-\ln\left(\frac{\hbar}{4eB_zL_\varphi^2}\right)\right] \tag{3}$$

where L_φ is the effective phase coherence length, Ψ is the digamma function, and α a parameter characterizing the number of independent coherent 2D conduction channels contributing to the magnetoresistance ($\alpha = 0.5$ for one conduction channel) [16]. As can be seen in Figure S8(a) the HLN model fits well the magnetoconductance data at low temperature up to several Teslas where the typical cusp shape is observed. The temperature dependence of the fitting parameters α and L_φ is shown in Figure S9. The extracted values of L_φ are all above the thickness of our film, confirming the validity of our 2D analysis.

We measure $\alpha \approx 0.5$ below 15 K and decreasing to 0.3 at higher temperature. The results from the fit thus show that there is only one 2D channel that contributes to the WAL at low temperature and that additional channels with no WAL contribution, possibly bulk channels, contribute to the magnetoresistance at temperature higher than 15 K, decreasing the α value. In an ideal topological insulator with a perfectly insulating bulk and uncoupled topological surface states (SSs), the expected value for α is 0.5 times the number of topological SSs. Including the top and bottom surface, α should be at least 1 or even larger in $Bi_{0.9}Sb_{0.1}$ due to its multiple surface conduction channels. Measuring α close to 0.5 suggests a strong coupling through the conducting bulk state in parallel with the topological SSs. As a consequence, the entire film acts as one 2D channel with α around 0.5. A similar value of α close to 0.5 was measured by several groups in topological insulators [17], whereas only electrostatic gating [18] or careful doping of the

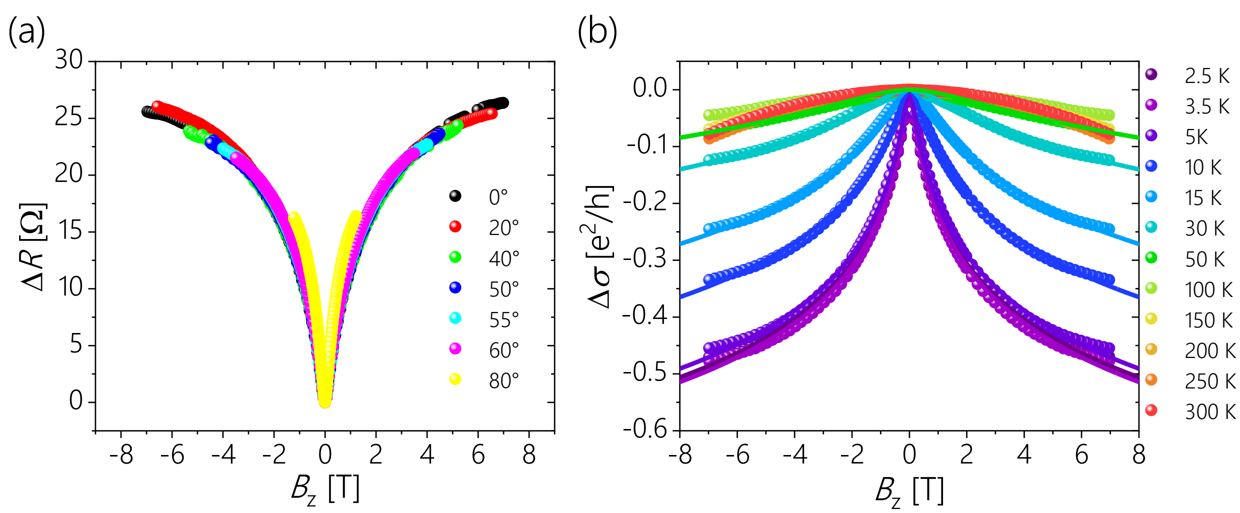

Figure S8: (a) Change of resistance ΔR as a function of B_z for different field angles at 2.5 K.(b) Magnetoconductance $\Delta\sigma$ normalized to the quantum of conductance e^2/h as a function of temperature. The solid lines are fits using the HLN model at low temperatures.

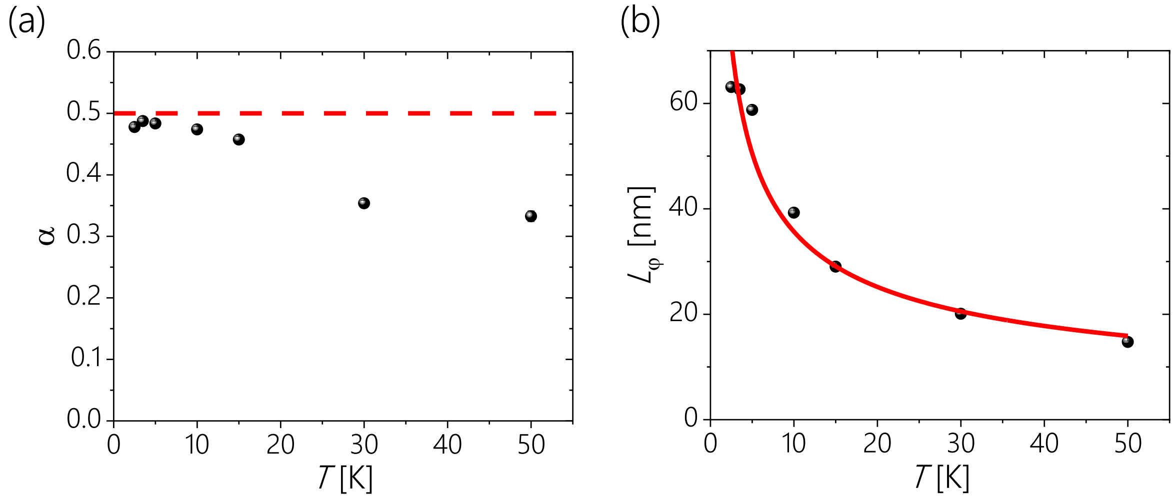

Figure S9: Temperature dependence of the parameters extracted from the HLN model: (a) α, the characteristic parameter related to the number of transport channels. The dashed line is the value expected for one conduction channel in 2D. (b) L_φ is the phase coherence length. The solid line is a fit using a power law $T^{-\beta}$.

topological insulator allows one to measure the contribution of single SSs [19].

The phase coherent length L_φ reaches up to 63.0±0.6 nm at 2.5 K and quickly decreases upon increasing the temperature. The phase coherence length is typical of topological insulator thin films at 2.5 K with results in the literature usually around 100 nm [17, 20, 21, 22]. The temperature dependence of L_φ can be fitted by a power law $T^{-\beta}$ with $\beta = 0.50 \pm 0.04$. The value of the exponent depends on the nature of the decoherence. In the 2D case $\beta = 1/2$ when the source of decoherence is the electron-electron scattering and $\beta = 1$ when it is the electron-phonon scattering. The obtained exponent evidences that the electron-electron scattering is the main scattering mechanism causing the decoherence [23].

References

[1] Fernando W. Gayanath. *Handbook of Metal Physics*. Vol. 4. Elsevier, 2008, pp. 89–110.

[2] K Malik et al. "Sb concentration dependent structural and resistive properties of polycrystalline Bi-Sb alloys". In: *Journal of Applied Physics* 112.8 (2012), p. 083706.

[3] K Sumiyama, T Sato, and GM Graham. "Thickness dependence of magnetization in Fe-Ni invar alloy film". In: *Solid State Communications* 19.5 (1976), pp. 403–404.

[4] YT Chen et al. "Magnetic properties of face-centered cubic Co films". In: *IEEE Transactions on Magnetics* 42.2 (2006), pp. 278–282.

[5] Can Onur Avci et al. "Unidirectional spin Hall magnetoresistance in ferromagnet/normal metal bilayers". In: *Nature Physics* 11.7 (2015), pp. 570–575.

[6] Yang Lv et al. "Large unidirectional spin Hall and Rashba- Edelstein magnetoresistance in topological insulator/magnetic insulator heterostructures". In: *Applied Physics Reviews* 9.1 (2022).

[7] Niklas Roschewsky et al. "Spin-orbit torque and Nernst effect in Bi-Sb/Co heterostructures". In: *Physical Review B* 99.19 (2019), p. 195103.

[8] Pan He et al. "Bilinear magnetoelectric resistance as a probe of three-dimensional spin texture in topological surface states". In: *Nature Physics* 14.5 (2018), pp. 495–499.

[9] Pan He et al. "Nonlinear planar Hall effect". In: *Physical review letters* 123.1 (2019), p. 016801.

[10] Aurelien Manchon et al. "Current-induced spin-orbit torques in ferromagnetic and antiferromagnetic systems". In: *Reviews of Modern Physics* 91.3 (2019), p. 035004.

[11] Can Onur Avci et al. "Interplay of spin-orbit torque and thermoelectric effects in ferromagnet/normal-metal bilayers". In: *Physical Review B* 90.22 (2014), p. 224427.

[12] Kevin Garello et al. "Symmetry and magnitude of spin–orbit torques in ferromagnetic heterostructures". In: *Nature nanotechnology* 8.8 (2013), pp. 587–593.

[13] Di Yue et al. "Spin-to-Charge Conversion in Bi Films and Bi/Ag Bilayers". In: *Physical Review Letters* 121.3 (2018), p. 037201.

[14] Taishi Chen et al. "Topological transport and atomic tunnelling–clustering dynamics for aged Cu-doped Bi2Te3 crystals". In: *Nature communications* 5.1 (2014), p. 5022.

[15] Shinobu Hikami, Anatoly I Larkin, and Yosuke Nagaoka. "Spin-orbit interaction and magnetoresistance in the two dimensional random system". In: *Progress of Theoretical Physics* 63.2 (1980), pp. 707–710.

[16] Matthew Brahlek et al. "Transport properties of topological insulators: Band bending, bulk metal-to-insulator transition, and weak anti-localization". In: *Solid State Communications* 215 (2015), pp. 54–62.

[17] T Guillet et al. "Magnetotransport in Bi2Se3 thin films epitaxially grown on Ge (111)". In: *AIP Advances* 8.11 (2018), p. 115125.

[18] Yong Seung Kim et al. "Thickness-dependent bulk properties and weak antilocalization effect in topological insulator Bi 2 Se 3". In: *Physical Review B* 84.7 (2011), p. 073109.

[19] AA Taskin et al. "Manifestation of topological protection in transport properties of epitaxial Bi 2 Se 3 thin films". In: *Physical review letters* 109.6 (2012), p. 066803.

[20] Saurav Islam et al. "Low-temperature saturation of phase coherence length in topological insulators". In: *Physical Review B* 99.24 (2019), p. 245407.

[21] Minhao Liu et al. "Electron interaction-driven insulating ground state in Bi 2 Se 3 topological insulators in the two-dimensional limit". In: *Physical review B* 83.16 (2011), p. 165440.

[22] Hadar Steinberg et al. "Electrically tunable surface-to-bulk coherent coupling in topological insulator thin films". In: *Physical Review B* 84.23 (2011), p. 233101.

[23] Juhn-Jong Lin and JP Bird. "Recent experimental studies of electron dephasing in metal and semiconductor mesoscopic structures". In: *Journal of Physics: Condensed Matter* 14.18 (2002), R501.